An olive oil phenolic is a new chemotype of mutant isocitrate dehydrogenase 1 (IDH1) inhibitors

Sara Verdura[1,2a], Elisabet Cuyàs[1,2a], Jesús Lozano-Sánchez[3,4a], Cristian Bastidas-Velez[2a], Laura Llorach-Parés[5], Salvador Fernández-Arroyo[6], Anna Hernández-Aguilera[6], Jorge Joven[6], Alfons Nonell-Canals[5], Joaquim Bosch-Barrera[2,7,8], Begoña Martin-Castillo[2,9], Luciano Vellon[10], Melchor Sanchez-Martinez[5], Antonio Segura-Carretero[3,4], Javier A. Menendez[1,2*]

[1] Program Against Cancer Therapeutic Resistance (ProCURE),

Metabolism and Cancer Group, Catalan Institute of Oncology, Girona, Spain

[2] Girona Biomedical Research Institute (IDIBGI), Girona, Spain

[3] Department of Analytical Chemistry, Faculty of Sciences, University of Granada, Granada, Spain

[4] Research and Development Functional Food Centre (CIDAF), PTS Granada, Granada, Spain

[5] Mind the Byte, Barcelona, Spain

[6] Unitat de Recerca Biomèdica, Hospital Universitari de Sant Joan,

IISPV, Rovira i Virgili University, Reus, Spain

[7] Department of Medical Sciences, Medical School, University of Girona, Girona, Spain

[8] Medical Oncology, Catalan Institute of Oncology, Girona, Spain

[9] Unit of Clinical Research, Catalan Institute of Oncology, Girona, Spain

[10]Stem Cells Laboratory, Institute of Biology and Experimental Medicine (IBYME-CONICET), Buenos Aires, Argentina.

[a] These authors contributed equally

*Corresponding author:

Javier A. Menendez

Catalan Institute of Oncology (ICO)
Girona Biomedical Research Institute (IDIBGI)
Edifici M2, Parc Hospitalari Martí i Julià, E-17190 Salt, Girona, Spain
Phone: + 34 872 987 087 Ext. 50; Fax: + 34 972 217 344
E-mail: jmenendez@iconcologia.net or jmenendez@idibgi.org

ABSTRACT

Mutations in the isocitrate dehydrogenase 1 (IDH1) gene confer an oncogenic gain-of-function activity that allows the conversion of α-ketoglutarate (α-KG) to the oncometabolite R-2-hydroxyglutaratye (2HG). The accumulation of 2HG inhibits α-KG-dependent histone and DNA demethylases, thereby generating genome-wide hypermethylation phenotypes with cancer-initiating properties. Several chemotypes of mutant IDH1/2-targeted inhibitors have been reported and some of them are under evaluation in clinical trials. However, the recognition of acquired resistance to such inhibitors within a few years of clinical use raises an urgent need to discover new mutant IDH1 antagonists. Here, we report that a naturally occurring phenolic compound in extra-virgin olive oil (EVOO) selectively inhibits the production of 2HG by neomorphic IDH1 mutations. *In silico* docking, molecular dynamics, including steered simulations, predicted the ability of the oleoside decarboxymethyl oleuropein aglycone (DOA) to preferentially occupy the allosteric pocket of mutant IDH1. DOA inhibited the enzymatic activity of recombinant mutant IDH1 (R132H) protein in the low micromolar range, whereas >10-fold higher concentrations were required to inhibit the activity of wild-type IDH1. DOA suppressed 2HG overproduction in engineered human cells expressing a heterozygous IDH1-R132H mutation. DOA restored the 2HG-suppressed activity of histone demethylases as it fully reversed the hypermethylation of H3K9me3 in IDH1-mutant cells. DOA epigenetically restored the expression of *PD-L1*, an immunosuppressive gene silenced in IDH1 mutant cells *via* 2HG-driven DNA hypermethylation. DOA selectively blocked colony formation of IDH1 mutant cells while sparing wild-type IDH1 isogenic counterparts. In sum, the EVOO-derived oleoside DOA is a new, naturally occurring chemotype of mutant IDH1 inhibitors.

Key words: IDH1, cancer, oncometabolites, olive oil, polyphenols

SUMMARY. An olive oil phenolic is a naturally occurring chemotype of mutant IDH1-targeted inhibitors that could be employed as a scaffold for drug discovery.

INTRODUCTION

Isocitrate dehydrogenase 1 (IDH1) is one of the very few metabolic enzymes identified to date in which single-point mutations are strongly associated with an increased risk of developing a number of malignancies, including glioma, acute myeloid leukemia (AML), chondrosarcoma, intrahepatic cholangiocarcinoma, angioimmunoblastic T-cell lymphoma, and prostate cancer (1-5). Cancer-associated mutational events in IDH1, the most frequent of which involve missense mutations of the active site arginine residue R132 (*e.g.*, R132H 395G > A substitution), disrupt the normal function of IDH1 to convert isocitrate to α-ketoglutarate (α-KG, also known as 2-oxoglutarate) while reducing NADP to NADPH and liberating CO_2. Instead, the mutations confer a neomorphic, gain-of-function activity for IDH1 to convert α-KG to the D isomer of 2-hydroxyglutarate (2HG, also known as (*R)*-2-hydroxyglutarate). The hallmark of IDH1-mutated cancer is thus the supraphysiological production of 2HG (6-8).

Because α-KG and 2HG share extensive structural similarity, 2HG operates as an oncometabolite that generates aberrant genome-wide hypermethylation phenotypes *via* the competitive inhibition of α-KG-dependent dioxygenases necessary for histone and DNA demethylation, such as jumonji-domain containing lysine histone demethylases (KDMs) and TET2 (9, 10). Thus, beyond the more general effects on redox states and DNA damage repair, a generally accepted consensus in the field is that IDH1 mutations are causal in the development and/or progression of various types of cancer due to a 2HG-driven epigenetic

rewiring, which impairs cellular differentiation and promotes the accumulation of self-renewing undifferentiated cells with tumor-initiating capacity (11-13).

Since the discovery in 2008 of a 2HG-producing IDH1 mutation as a target for personalized anti-cancer therapy, a number of compounds capable of reducing 2HG levels by specifically targeting the neomorphic activity of mutant IDH1 enzymes have been developed (6, 7, 14). Several clinical trials are under way to assess the efficacy of at least four inhibitors targeting mutant IDH1 (AG-120, IDH-305, FT-2102, and BAY-1436032) and one pan-inhibitor targeting both mutant IDH1 and IDH2 (AG-881) in advanced hematological and solid tumors. Early results have provided compelling clinical proof-of-concept validating the two unique aspects that make the development of small-molecule inhibitors of mutant IDH1 attractive: namely, the expected non-interference with wild-type (WT) IDH1 enzyme activity and the absence or minimal toxicity expected from removing 2HG, which apparently lacks any physiological function. However, we are beginning to appreciate that non-responding patients can exhibit 2HG suppression, suggesting that removal of 2HG might not be sufficient to successfully reverse cell transformation by mutant IDH1 (6, 15-23). Perhaps more importantly, the rapid recognition of acquired resistance within a few years of clinical use of IDH-targeted inhibitors, a phenomenon that has recently been described to involve second-site mutations and recurrent increase in 2HG production (16), raises an urgent need to discover different chemotypes of mutant IDH1 antagonists.

We recently showed that decarboxymethyl oleuropein aglycone (DOA), a phenol-conjugated oleoside present in extra-virgin olive oil (EVOO), can target undifferentiated cellular states with tumor-initiating capacity (24). Here, we undertook a systematic *in silico* and *in vitro* approach to test the ability of DOA to specifically inhibit the neomorphic activity of mutant IDH1 (R132H), reduce 2HG production, reverse 2HG-driven rewiring of epigenetic and immunological landscape, and restrain 2HG-enhanced tumor-initiating capacity.

MATERIALS and METHODS

Computational modeling of IDH1. The IDH1 conformation to model WT IDH1 was 1T0L, which represents the crystal structure of IDH1 in complex with NADP, isocitrate, and Ca^{2+} (25). The IDH1 conformations to model mutant IDH1 R132H were the following: 4UMX, a crystal structure of a selective allosteric inhibitor of mutant IDH1 (i.e., the bis-imidazole phenol cpd1) complexed with mutant R132H IDH1 (26); 4KZO, a crystal structure of mutant R132H IDH1 in complex with $NADP^+$ and Ca^{2+}/α-KG (26); 5LGE, a crystal structure of mutant R132H IDH1 in complex with $NADP^+$ and an inhibitor related to the pan-mutant IDH1 inhibitor BAY 1436032 (27); 3INM, a crystal structure of mutant R132H IDH1 in complex with NADPH, α-KG and Ca^{2+} (28); 6B0Z, a crystal structure of mutant R132H IDH1 in complex with the 3-pyrimidine-4-yl-oxazolidin-2-ones mIDH1 inhibitor IDH305 (29); 5TQH, a crystal structure of mutant R132H IDH1 in complex with the (S,S)-oxazolidinone mIDH1 inhibitor IDH889 (30); 5SVF and 5SUN, two crystal structures of mutant R132H IDH1 in complex with the allosteric mIDH1 inhibitors IDH125 and IDH146, respectively (31); 5DE1, a crystal structure of mutant R132H IDH1 in complex with the mutant IDH1 inhibitor GSK321A (32); 3MAP, a crystal structure of mutant R132H IDH1 in complex with NADP and isocitrate (33); 4XRX and 4XS3, two crystal structures of mutant R132H IDH1 in complex with 2-thiohydantoin-related compounds (34); and 4I3K, a crystal structure of mutant R132H IDH1 in complex with 1-hydroxypyridin-2-one compounds (35). The IDH1 conformations to model G97D IDH1 were 4L03 and 4L04, two crystal structures of mutant G97D IDH1 in complex with $NADP^+$, and Ca^{2+}/α-KG (36). Finally, 3MAS, a crystal structure of heterodimeric mutant R132H IDH1 (chain A) and WT IDH1 (chain B) in complex with NADP and isocitrate, was employed to model WT IDH1:R132H mutant IDH1 heterodimers (33).

The biological assembly of all the aforementioned WT/mutant IDH1 conformations co-crystalized with the substrate, the cofactor, and/or an allosteric inhibitor, took place in a dimeric form, and such conformation was maintained when performing docking and

molecular dynamics (MD) simulations. However, because the orthosteric pocket is identical in both chains, we only analyzed the catalytic pocket in the best-resolved chain or, when the resolution was similar in both chains, in that of the chain A. In the case of 3MAS, both catalytic pockets were evaluated because each one belongs to the WT and the R132H mutant conformation. Therefore, all the docking and MD calculations were performed in two cavities per each WT/mutant IDH1 conformation. When calculations were carried out over the allosteric pocket, substrates and/or cofactors were maintained if they were co-crystalized in the structure. Conversely, substrates and/or cofactors were eliminated when the calculations involved the catalytic pockets.

Docking calculations. All docking calculations were performed using Itzamna and Kin (www.mindthebyte.com), which are classical docking and blind-docking software tools (37). The aforementioned protein structures from the Research Collaboratory for Structural Bioinformatics PDB were directly employed for docking calculations using the orthosteric and allosteric cavities of IDH1 defined by crystallographic ligands where available. Two runs were carried out for each calculation to avoid false positives.

Molecular dynamics simulations. Docking post-processing allowing conformational selections/induced fit events to optimize the interactions were performed *via* short (1 ns) MD simulations using NAMD version 2.10 over the best-docked complexes, which were selected based on the interaction energy. The Ambers99SB-ILDN and the GAFF forcefield set of parameters were employed for IDH1 and DOA, respectively. The GAFF parameters were obtained using Acpype software, whereas the IDH1 structures were modeled using the leap module of Amber Tools. Simulations were carried out in explicit solvent using the TIP3P water model with the imposition of periodic boundary conditions *via* a cubic box. Electrostatic interactions were calculated by the particle-mesh Ewald method using constant pressure and temperature conditions. Each complex was solvated with a minimum distance of 10 Å from the surface of the complex to the edge of the simulation box; Na^+ or Cl^- ions were also added to the simulation to neutralize the overall charge of the systems. The temperature was maintained at 300 K using a Langevin thermostat, and the pressure was maintained at 1 atm using a Langevin Piston barostat. The time step employed was 2 fs. Bond lengths to hydrogens were constrained with the SHAKE algorithm. Before production runs, the structure was energy minimized followed by a slow heating-up phase using harmonic position restraints on the heavy atoms of the protein. Subsequently, the system was energy minimized until volume equilibration, followed by the production run without any position restraints.

Binding free energy analysis. Molecular Mechanics/Generalized Borne Surface Area (MM/GBSA) calculations were performed to calculate the alchemical binding free energy (ΔG_{bind}) of DOA against IDH1. MM/GBSA rescoring was performed using the MMPBSA.py algorithm within AmberTools. The snapshots generated in the 1 ns MD simulation were imputed into the post-simulation MM/GBSA calculations of binding free energy. Graphical representations were prepared using PyMOL program and PLIP version 1.3.0.

Interaction analysis. The predicted binding site residues of DOA to IDH1 were defined using evidence-based interaction analyses of known mutant IDH1 inhibitors with well-defined binding residues in the orthosteric and allosteric cavities.

Steered molecular dynamics simulations. In steered MD (SMD) simulations, a time-dependent external force was applied to DOA from an internal atom of the IDH1 protein, thereby allowing a detailed analysis of its unbinding process. SMD simulations were performed using NAMD version 2.11, with the last frame obtained from the post-processing MD simulation used as input. 1T0L was employed as the model for the DOA-WT IDH1 complex whereas 3MAP and 4L04 were used as the best conformations for DOA-mutant IDH1 complexes in terms of binding energy to the orthosteric and allosteric cavities, respectively. A harmonic constraint force constant of 4 kcal/mol/Å with a constant velocity of 0.00002 Å/ns was applied using the following direction vectors: 1T0L (0.3173912335710011, 0.16624967558395973, 0.9336079745913197), 3MAP (0.8623143751518405, -0.2165225950454174, 0.4577465283771023), and 4L04 (0.8995843287735461,0.005154534447021301,-0.4367166887121249). The time length evaluation for each simulation was 1 ns, using a time-step of 2 fs, which was sufficient to evaluate the entire DOA unbinding process from the orthosteric/allosteric cavities of IDH1. The remainder of the parameters was the same as those above-mentioned for MD simulations. The generated trajectory was finally evaluated using VMD to extract the exerted force (pN) per simulation frame.

DOA isolation and purification. DOA was isolated and purified from the phenolic fraction of EVOO as described previously (24).

IDH1 activity/inhibition enzymatic assays. The enzymatic studies of recombinant WT-IDH1 (BPS#71075, lot#101019) and IDH1 R132H (BPS#71099, lot#170222-2) were outsourced to BPS Bioscience (San Diego, CA). Briefly, DOA was diluted in 10% DMSO and 20 μl of the dilution was added to a 200 μl reaction buffer to ensure that the final concentration of DMSO was 1% all of the reactions.

For the WT IDH1 enzyme, the 200 μL reaction mixture contained 50 mmol/L Tris (pH 7.4), 10 mmol/L $MgCl_2$, 200 μmol/L DL-isocitrate, 200 μmol/L NADP and WT IDH1 (50 ng). For the R132H IDH1 mutant enzyme, the 200 μL reaction mixture contained 25 mmol/L Tris (pH 7.4), 10 mmol/L $MgCl_2$, 150 mmol/L NaCl, 0.3 mg/mL bovine serum albumin, 1 mmol/L α-KG, 10 μmol/L NADPH and R132H IDH1 (600 ng). The enzymatic reactions were performed at room temperature (RT) and monitored continuously for 20 min at 340 nm using absorption spectrometry. Absorption was read with a microplate reader (Tecan Infinite M1000, Tecan Group, San Jose, CA).

WT IDH1 and R132H IHD1 activity assays were performed in duplicate at each DOA concentration. The absorption data were analyzed using Graphpad Prism. The difference between ΔAbs in the absence of IDH (ΔAbs_t) and in the presence of IDH (ΔAbs_c) was defined as 100% activity (ΔAbs_t - ΔAbs_c). Using absorption (ΔAbs) in the presence of the compound, % activity was calculated as: % activity = [(ΔAbs_t – ΔAbs)/(ΔAbs_t – ΔAbs_c)] x 100%, were ΔAbs = the absorption in the presence of the compound (all percent activities below zero were computed also in a table of activities), and where ΔAbs = (Abs at $_{time=t}$) – (Abs at $_{time=0}$) for WT IDH1 and ΔAbs = (Abs at $_{time=0}$) – (Abs at $_{time=t}$) for R132H IDH1.

Cell lines. X-MAN™ isogenic cell lines were obtained from Horizon Discovery Ltd. (Cambridge, UK). The X-MAN™ isogenic cell lines MCF10A and HCT116$^{R132H/WT}$ heterozygous knock-in of *IDH1* dominant-negative R132H point mutation (cat. # HD 101-013 and HD 104-021, respectively), were used in this study. The parental cell lines MCF10A and HCT116 (*IDH1*$^{WT/WT}$) served as controls. Cells were maintained according to the supplier's recommendations: DMEM/F-12 including 2.5 mmol/L L-glutamine and 15 mmol/L HEPES, supplemented with 5% horse serum, 10 µg/mL insulin, 20 ng/mL hEGF, 0.5 µg/mL hydrocortisone, 0.1 µg/mL cholera toxin for MCF10A cells and RPMI 1640 including 2 mmol/L L-glutamine and 25 mmol/L sodium bicarbonate, supplemented with 10% fetal bovine serum for HCT116 cells. Cell lines were authenticated by STR profiling, both performed by the manufacturer and confirmed in- house at time of purchase using ATCC guidelines. Cells were passaged by starting a low-passage cell stock every month up to 3 months after resuscitation. Cell lines were regularly screened for *Mycoplasma* contamination using a MycoAlert Mycoplasma Detection Kit (Lonza, Verviers, Belgium).

Quantification of 2-hydroxyglutarate. The concentration of 2HG in cell lysates from cells cultured in the absence or presence of graded concentrations of DOA for 48 h was determined using the D-2-Hydroxyglutarate Assay Kit (colorimetric assay; ab211070) performed as per the manufacturer's instructions (Abcam plc; Cambridge, UK). Quantitative measurements of 2HG were performed also by employing a method based on gas chromatography coupled to a quadrupole time-of-flight mass spectrometer and an electron impact interface (GC-EI-QTOF-MS). A detailed description of this procedure is given in Cuyàs *et al*. (38) and Riera-Borrull *et al.* (39).

H3K9me3 western blotting. For western blot analyses of H3K9me3, histones from whole-cell lysates were electrophoresed on 15% SDS-PAGE gels, transferred to nitrocellulose membranes, and incubated with an antibody against H3K9me3 (Abcam; cat.#ab8898, 1:1,000 dilution), followed by horseradish peroxidase-conjugated secondary and chemilumiscence detection. Blots were reprobed with an antibody for β-actin to control for protein loading and transfer.

H3K9me3 indirect immunofluorescence. Cells plated onto glass coverslips were fixed with 4% paraformaldehyde in phosphate buffered saline (PBS). Following fixation at RT for 5 min,

the cells were permeabilized with 0.1% Triton X100/PBS. The coverslips were placed in the antibody solution and incubated for 60 min at RT. The cells were then washed and stained with secondary antibody. Nuclei were counterstained with Hoechst 33342. Images were obtained with a Nikon Eclipse 50i fluorescence microscope including NIS-Elements imaging software. Images were noise-filtered, corrected for background, and prepared using Adobe Photoshop.

RNA isolation and reverse transcription. Total RNA was extracted from cells using Nucleospin RNA plus kit (Macherey-Nagel GmbH & Co. KG Düren, Germany). Two micrograms of total RNA was reverse-transcribed into cDNA using the High Capacity cDNA Reverse Transcription Kit (Thermo Fisher Scientific, Carlsbad, CA). RNA concentration and quality were determined with an ND-1000 spectrophotometer (NanoDrop™ ND-1000, NanoDrop Technologies, Wilmington, DE).

***PD-L1* gene expression.** cDNA (20 ng) was assayed in triplicate according to established protocols using a QuantStudio™ 7 Flex Real-Time PCR system (Thermo Fisher Scientific, Waltham, MA) with an automated baseline and threshold cycle detection. *GAPDH* and *ACTB* were used as reference genes. Primers and fluorescent probes for PD-L1, GAPDH, and 18S were obtained from Thermo Fisher Scientific (TaqMan Gene Expression assay IDs: Hs01125301_m1, Hs99999905_m1, and Hs99999901_s1, respectively). Data were analyzed using the Thermo Fisher Cloud software.

Flow cytometry. The specific surface expression of PD-L1 was determined by flow cytometry by measuring the binding of a PE-labeled mouse anti-PD-L1/CD274 antibody (cat#557924, BD Biosciences-US) and using the PE-labeled mouse IgG_1, κ as isotype control (cat#555749) as per the manufacturer's instructions. Flow cytometry analysis was performed with a BD Accuri C6 Flow Cytometer (BD Biosciences). The mean fluorescence signal associated with cells for labelled PD-L1 was quantified using the fluorescence parameter provided with the BD Accuri C6 software.

Metabolic status assessment. Cell viability was determined using standard colorimetric MTT-based reduction assays.

Colony formation assays. Anchorage-dependent clonogenic growth assays were performed by initially seeding MCF10A R132H/+ and MCF10A *IDH1*$^{WT/WT}$ cells into six-well plates at very low densities (~100 cells/well) and cultured in the presence or absence of graded concentrations of DOA for 7 to 10 d (without refeeding) in a humidified atmosphere with 5% CO_2, at 37°C. Alternatively, cells were either left untreated or treated for 48 h with graded concentrations of DOA. Cells were then replated in six-well plates (~100 cells/well) and cultured in drug-free medium for 7 to 10 d as before. Colonies were stained with crystal violet and the number of colonies with >50 cells/each were counted. ImageJ was used to quantify the size of colonies.

Statistical analysis. All statistical analyses were performed using XLSTAT 2010 (Addinsoft™, New York, NY). For all experiments, at least two independent biological replicates were performed with n ≥3 technical replicates per experiment. No statistical method was used to predetermine sample size. Investigators were not blinded to data allocation and experiments were not randomized. Data are presented as mean ± S. D. Two-group comparisons were performed using Student's *t* test for paired and unpaired values. Comparisons of means of ≥3 groups were performed by ANOVA, and the existence of individual differences, in case of significant *F* values at ANOVA, were tested by Scheffé's multiple contrasts. All statistical tests were two-sided.

RESULTS

During a computational de-orphanization of the biomolecular targets of DOA, a virtual profiling (VP) approach employing the structure-based software tool *Ixchel* (www.mindthebyte.com) (a structure-based VP tool that performs docking calculations of a molecule -SDF or SMILE file- against an *in-house* developed database comprising almost 9,000 binding sites protein cavities curated from RSCB PDB according to UniProtKB human entries and returns the binding energy of every possible interaction (37)) was capable of identifying 996 putative DOA targets based on a binding energy significance threshold of -6.0 kcal/mol (*manuscript in preparation*). Such list of predicted targets for DOA was significantly enriched with epigenetic (e.g., HDACs, HMTs, SIRTs, KDMs, etc) and metabolic (e.g., NAMPT, NNMT, COMT, MTHFD1, etc) enzymes. Among them was the PDB ID 4L03, which corresponds to the homodimeric form of G79D IDH1, a rare clinical form of mutant IDH1 that overproduces the 2HG oncometabolite (36). Because crystallographic structural studies have demonstrated that distinct chemotypes developed against specific forms of mutant IDH1 might exert cross-inhibitory activities against other mutant enzymes (7), we hypothesized that the *in silico* predicted ability of DOA to target the rarer IDH1 G79D mutant might also involve the most frequently observed IDH1 mutation, R132H.

DOA is computationally predicted to target IDH1. To gain *in silico* insight into the putative mode of binding of DOA to WT and mutant IDH1 (i.e., WT IDH1 homodimers, R132H IDH1:R132H IDH1 homodimers, G79D IDH1:G79D IDH1 homodimers, and WT IDH1:R132H IDH1 heterodimers), we employed seventeen different crystal structures of IDH1 that were selected after a search of the PDB database: namely, 1T0L for homodimeric WT IDH1, 4UMX, 4KZO, 5LGE, 3INM, 6B0Z, 5TQH, 5SVF, 5SUN, 5DE1, 3MAP, 4XRX, 4XS3, and 4I3K for homodimeric R132H IDH1, 4L03 and 4L04 for homodimeric G79D IDH1, and 3MAS for heterodimeric WT IDH1:R132H IDH1.

Rigid docking calculations were performed over the cavities defined by the

crystallographic ligands. In the case of structures lacking substrates or inhibitors, the binding region was delineated by analogy using the existing pockets from the available crystallographic structures as templates. After simulations, we selected the best interacting poses based not only on the computed interaction energy, but also on the crystallographic binding poses of the ligands reported in the literature (**Supplementary Fig. S1**). To add protein flexibility to the analysis and to test the stability of the selected DOA-target complexes, we additionally carried out short MD simulations of 1 ns to filter out poorly interacting poses (**Supplementary Fig. S2**). We then performed MM/GBSA calculations (40) to estimate the free energy of the binding of DOA to the orthosteric and allosteric cavities of IDH1. MM/GBSA-based estimation of ligand-binding affinities take into consideration the dynamic nature of the accommodation of DOA to IDH1 and is therefore more reliable to provide a realistic view of the binding affinity of DOA than rigid docking estimations. The energies obtained following MM/GBSA rescoring calculations over MD simulations are summarized in **Supplementary Table S1**. For the catalytic region, the best DOA binding energies occurred with the R132H homodimers 3MAP and 4KZO; for the allosteric cavity, however, the best DOA binding energies occurred with the R132H homodimer 3INM and the G97D homodimer 4L04. Remarkably, a majority of the best binding energies were predicted to occur on crystallographic structures exhibiting an active, closed state of the IDH1 protein. Since the closed conformations of mutant IDH1 proteins are still active (whereas open conformations are inactive), these results tend to validate the notion that DOA could exhibit some selectivity against the active, mutant conformations of IDH1.

Binding mode of DOA to IDH1. To characterize the binding mode of DOA to IDH1, we evaluated and compared it across all the conformations and against all the key residues existing at the orthosteric and allosteric pockets (**Fig. 1A**). First, we performed a comprehensive bibliographic and PLIP-based examination of all the substrate/cofactors and IDH1 inhibitor interactions for each of the 17 crystallographic structures evaluated. Once the key binders were delineated, we performed an interaction study against DOA over the orthosteric and allosteric cavities, assembling a list of shared interactions between DOA, substrate/cofactors, and IDH1 inhibitors (**Supplementary Table S2**). We finally defined the key interactions by considering solely those that were in agreement with earlier studies, remaining present upon MD simulations, and were repeated in a majority of the crystallographic structures. The key interacting residues that delineate DOA's binding mode to the orthosteric/catalytic cavity of IDH1 were K72, T75, T77, N96, T311, and V312 (**Fig. 1A**). The key interacting residues that delineate DOA's binding mode to the allosteric cavity of IDH1 were L120, W124, I128, W267, and V281 (**Fig. 1A**). A careful analysis of the DOA-

IDH1 interactions concluded that the key interacting residues were more conserved at the allosteric cavity. For one of the adopted conformations (4XRX), the rigid docking analysis established T77 and N96 as key interactions; however, these were lost after MD simulations. This type of finding, along with the tendencies in the binding energies, appear to suggest that DOA could perform more relevant interactions with key residues at the allosteric cavity of IDH1. Such an analysis also revealed that the key interacting residues were less conserved in the case of WT IDH1 (1T0L) than in mutant IDH1 structures.

For the catalytic cavity, three key interactions were predicted to occur in the WT IDH1 1T0L crystallographic structure (A74, R132, and T311), whereas five residues, T75, H132, I251, Q283, and A307, were predicted to be involved in the binding with the mutant IDH1 3MAP crystallographic structure, which was the conformation with the best binding energy of DOA at the catalytic region of IDH1. In general, the interactions shared by DOA with the substrate/cofactor at the orthosteric cavity in a majority of the IDH1 structures were T311 and T75, which were shared in 7 out of 18 conformations analyzed (**Supplementary Table S2**). Another three residues (T77, V312, and N96), which were present in 3 or 4 out of 18 conformations analyzed, were also predicted to play an important role in the binding mode of DOA at the orthosteric cavity of IDH1. Therefore, the five more frequent residues are in close agreement with those predicted as the key binders in the orthosteric cavity. In the case of the allosteric cavity, DOA was predicted to establish three out of five interactions predicted as key with both the WT IDH1 1T0L structure and the 3INM conformation, that is, the mutant IDH1 structure with the best binding energy of DOA at the allosteric pocket. In general, the interactions shared by DOA with known IDH1 inhibitors at the allosteric cavity in a majority of the IDH1 structures were I128, W124, V281, W267, and L120, in complete agreement with those predicted as key interacting residues. Indeed, some of these interactions were shared by nine (I128, W124), seven (V281, W267), and five (I120) of the IDH1 conformations evaluated. Overall, these findings strongly suggest that from a structural perspective it seems difficult to establish clear differences between the WT and the mutant forms of IDH1. Moreover, the allosteric cavity was once again predicted to behave as the preferred targeted cavity of DOA against IDH1.

DOA might preferentially bind the allosteric cavity of IDH1. To reinforce the cavity preference of DOA against IDH1 beyond binding energies, we computationally calculated the dissociation constant, K_d (**Supplementary Table S1**), which is inversely proportional to the binding constant – the higher the binding energy and the lower the binding constant, the better the inhibitory effect of the molecule. This approach revealed that DOA was predicted

to bind better to the allosteric cavity of IDH1 in all the crystallographic structures evaluated with the exception of 4I3K and 4KZO.

To provide a higher degree of computational strength to the predicted ability of DOA to preferential target the allosteric cavity of IDH1, we carried out SMD simulations inspired by the atomic force microscopy technique, which have been used extensively to evaluate the binding properties of biomolecules and their response to external mechanical manipulations. Briefly, a time-dependent external force is applied to force the unbinding of a ligand (in this case DOA) from a given cavity, and both the magnitude and the average velocity of the ligand unbinding can be calculated to estimate not only the strength of the binding, but also the computational residence time which, when used together, can better inform on the inhibitory activity of a given ligand (DOA) towards a given cavity. SMD simulations where performed with the 1T0L WT IDH1 structure as well as with 3MAP and 4L04, the best conformations of mutant IDH1 in terms of binding energy of DOA to the orthosteric and allosteric cavities, respectively. As shown in **Fig. 1B** (*top panel*), although similar forces were needed to remove DOA from the orthosteric cavity of WT IDH1 (1T0L) and mutant IDH1 (3MAP), a longer computational residence time can be observed in the latter case. As shown in **Fig. 1B** (*middle panel*), the force needed to remove DOA from the allosteric cavity of mutant IDH1 (4L04) was 20 pN higher than that needed to remove DOA from the allosteric cavity of WT IDH1 (1T0L), and about 200 pN higher than that calculated to unbind DOA from the orthosteric cavity of IDH1. Moreover, the computational residence time of DOA was ~150 fs longer in the mutant IDH1 (4L04) structure than in WT IDH1 (1T0L), but equivalent to that calculated for the orthosteric cavity. These findings, together with the binding energies, interaction analyses and K_d values, once again predict that DOA might preferentially target the allosteric cavity at the mutant forms of IDH1, specifically the most commonly occurring R132H (**Fig. 1B,** *bottom panel*).

DOA selectively inhibits mutant IDH1 activity *in vitro.* To test the selective inhibitory activity of DOA against R132H IDH1, we performed enzyme activity assays with purified, recombinant R132H IDH1 and WT IDH1 proteins. DOA treatment dose-dependently inhibited the capacity of R132H IDH1 to catalyze the reduction of α-KG to 2HG using NADPH as the cofactor, with an IC_{50} value of ~12 μmol/L (**Fig. 2A**). Conversely, we failed to calculate the IC_{50} value of DOA against the WT IDH1-catalyzed conversion of isocitrate using NADP as the cofactor, even when using the highest concentration of DOA tested in the assay (100 μmol/L; **Fig. 2A**).

DOA inhibits mutant IDH1-catalyzed 2HG production *in vivo*. Encouraged by the promising inhibitory activity of DOA against the neomorphic enzymatic function of R132H IDH1 *in vitro*, we next determined its impact on 2HG production in MCF10A breast epithelial cells engineered to express a heterozygous knock-in of the *IDH1*^{R132H} mutation. After treatment with various concentrations of DOA or DMSO as a vehicle control for 48 h, the inhibition of the aberrant biological activity of R132H IDH1 was tested by indirectly measuring the concentration of 2HG in cell lysates using a colorimetric assay. In this assay, 2HG is oxidized to α-KG in the presence of 2HG dehydrogenase and substrate mix; the intermediate product reduces the probe to a colored product with strong absorbance at 450 nm, which is proportional to the amount of 2HG in the samples. DOA was as efficient as the IDH1 inhibitor AGI-5198 at suppressing 2HG overproduction in MCF10A$^{R132H/WT}$ cells, with levels returning to the almost undetectable baseline levels of MCF10A$^{WT/WT}$ parental counterparts (**Fig. 2B**).

To confirm the ability of DOA to inhibit the mutant IDH1 enzyme *in vivo*, we performed a secondary validation using MS in extracts of cells treated with DOA. As anticipated, quantitative measurements of 2HG by GC-EI-QTOF-MS revealed that DOA treatment considerably decreased the overproduction of 2HG by ~85% in MCF10A$^{R132H/WT}$ cells (**Fig. 2B**). ELISA-based and MS-based approaches confirmed that DOA treatment was similarly capable of decreasing 2HG overproduction in HCT116$^{R132H/WT}$ cells (**Supplementary Fig. S3A**).

DOA inhibits 2HG-driven histone hypermethylation. To corroborate that the sole excess of the oncometabolite 2HG in an otherwise isogenic background was sufficient to increase histone methylation through inhibition of jumonji lysine demethylases, we compared the pattern of trimethylated histone 3 lysine 9 (H3K9me3) in MCF10A$^{R132H/WT}$ and MCF10A$^{WT/WT}$ parental cells. Western blot analysis confirmed that the global level of H3K9me3 was considerably higher in 2HG-overproducing MCF10A$^{R132H/WT}$ knock-in cells than in MCF10A$^{WT/WT}$ cells, which is consistent with 2HG-induced broad inhibition of histone demethylation (41-43, **Fig. 3A**, *left*). Upon confirming the ability of DOA to inhibit mutant IDH1 *in vivo*, we next questioned whether DOA could restore the activity of histone demethylases and consequently reduce the levels of histone lysine methylation. Treatment of MCF10A$^{R132H/WT}$ cells with DOA fully suppressed the tri-methylation of H3K9 while failing to alter the baseline status of H3K9me3 in MCF10A$^{WT/WT}$ cells (**Fig. 3A**, *left*). Indirect immunofluorescence analyses confirmed a striking accumulation of H3K9me3 in nuclei of MCF10A$^{R132H/WT}$ cells compared with MCF10A$^{WT/WT}$ cells (**Fig. 3A**, *right*), likely indicating

2HG-induced inhibition of JMJD2A/KDM4A (44) in MCF10A$^{R132H/WT}$ cells. In the presence of DOA, nuclear H3K9me3 signals in MCF10A$^{R132H/WT}$ cells returned to near-baseline levels found in MCF10A$^{WT/WT}$ cells (**Fig. 3A**, *right*). Although we failed to observe an increase in H3K9me3 levels in 2HG-overproducing HCT116$^{R132H/WT}$ cells, it was noteworthy that DOA potently and selectively suppressed the tri-methylation levels of H3K9 in HCT116$^{R132H/WT}$ cells but not in HCT116$^{WT/WT}$ cells (**Supplementary Fig. S3B**).

DOA reverses 2HG-induced epigenetic suppression of PD-L1. The accumulation of 2HG in IDH1 mutated cells has been suggested to impact the immune landscape by manipulating the expression of the checkpoint ligand PD-L1 (23). To evaluate whether the sole excess of 2HG in an otherwise isogenic background was sufficient to alter the constitutive expression of PD-L1, we quantified mRNA and protein levels for PD-L1 by real-time PCR and flow cytometry, respectively. As expected, PD-L1 expression was significantly lower in MCF10A$^{R132H/WT}$ cells than in MCF10A$^{WT/WT}$ counterparts (**Fig. 3B**, *left panels*). To evaluate whether this change involved changes to DNA methylation, *PD-L1* mRNA was quantified by real-time PCR in the absence or presence of 5-azacytidine (5-aza), a DNA methyltransferase (DNMT) inhibitor that is known to induce genome-wide non-specific hypomethylation. *PD-L1* mRNA expression was strongly up-regulated by 5-aza treatment not only in 2HG-overproducing MCF10A$^{R132H/WT}$ cells (~6-fold increase) but also in MCF10A$^{WT/WT}$ cells (~3-fold increase). Treatment with DOA, which is known to inhibit DNMT1 (24), was as efficient as 5-aza at up-regulating *PD-L1* mRNA expression in both WT IDH1- and mutated IDH1-expressing cells (**Fig. 3B**, *left panels*).

Having established that *PD-L1* gene expression was dynamically affected by the DNA methylation status of cells irrespective of the IDH1 mutation status, we sought to determine whether pharmacological inhibition of mutant IDH1 enzymatic activity would suffice to augment the population of PD-L1-positive cells and/or to up-regulate the expression of *PD-L1* per cell. A significantly lower number of PD-L1-positive cells (48%) was found in the MCF10A$^{R132H/WT}$ cell population as compared with MCF10A$^{WT/WT}$ counterparts, in which almost 90% of the cells were PD-L1 positive. DOA was as efficient as the mutant IDH-targeted specific inhibitor AGI-5198 at promoting a significant increase in the number of PD-L1-positive cells in MCF10A$^{R132H/WT}$ cell populations. Indeed, DOA- and AG-5198-treated MCF10A$^{R132H/WT}$ cultures phenocopied the number of PD-L1-positive cells observed in MCF10A$^{WT/WT}$ parental cells (~90%). When we evaluated changes in the mean fluorescence intensity, we observed that DOA, but not AGI-5198 enhanced PD-L1-associated cell surface expression in both WT IDH1 and mutant IDH1 cells (**Supplementary Fig. S3C**).

DOA inhibits colony formation in mutant IDH1 cells. With evidence of DOA blocking the mutant IDH1 enzyme activity, decreasing 2HG production, and suppressing some of the 2HG-driven epigenetic aberrations in IDH1-mutant cells, we finally assessed whether this translated into the ability to inhibit 2HG-enhanced tumorigenic activity. To measure clonogenic survival, cells were seeded in 6-well plates at a density of 100 cells/well and were then cultured in the presence or absence of graded concentrations of DOA for 7 d without replenishment of the compound. Clonal growth analyses demonstrated a slightly more pronounced dose-dependent inhibition of colony formation accompanied by a significant reduction of colony size in DOA-treated MCF10A$^{R132H/WT}$ cells as compared with DOA-treated MCF10A$^{WT/WT}$ isogenic counterparts (**Fig. 4**). When DOA was tested in parallel for its effects on cell viability**,** the results showed that its ability to differentially decrease the capacity of MCF10A$^{R132H/WT}$ cells to generate clones long-term could not be explained in terms of early, general cytotoxicity (**Supplementary Fig. S3D**). In another approach, HCT116$^{WT/WT}$ and HCT116$^{R132H/WT}$ cells were treated for 48 h with a non-cytotoxic concentration of DOA and, following treatment, cells that remained attached were collected and seeded into 6-well plates at a density of 100 cells/well. Such pre-treatment with DOA sufficed to notably decrease the clonogenic potential of 2HG-overproducing HCT116$^{R132H/WT}$ cells without notably affecting the colony formation capacity of the HCT116$^{R132H/WT}$ counterparts (**Supplementary Fig. S3E**).

DOA is a new chemotype of mutant IDH1-targeted inhibitors. On the basis of the similar property principle (45), which states that structurally related molecules are more likely to have comparable properties and biological activities, we employed 2D and 3D molecular fingerprints to disentangle whether DOA functioned as a mutant IDH1-targeted inhibitor by mimicking either IDH1 crystallographic ligands or small-molecule inhibitors of mutant IDH1. When pairwise similarity calculations were measured using Dice and Tanimoto indexes (46 **Fig. 5**), we failed to observe a significant 2D structural resemblance between DOA, IDH1 substrates (isocitrate [ICT], citrate anion [FLC], α-ketoglutarate [AKG]), IDH1 cofactors (NADPH [NDP], NADP+ [NAP]), and a wide representation of currently existing mutant IDH1-targeted inhibitors (47). Also, 3D similarity searches failed to identify significant physicochemical similarities between DOA, IDH1 substrates/cofactors and IDH1 antagonists (**Fig. 5**).

DISCUSSION

A limited number of chemotypes capable of inhibiting the neomorphic activity of mutant IDH1 in cancer cells are currently available. Here, we provide *in silico* and *in vitro* evidence to suggest that the oleoside DOA, a phenol-conjugated molecule from EVOO, is a naturally occurring inhibitor of cancer-associated mutant IDH1 that could be employed as a scaffold for drug discovery of new mutant IDH1-targeting compounds.

Our *in silico* approach involving docking, MD and SMD simulations predicted that DOA might behave as an inhibitor of mutant IDH1 by preferentially targeting the allosteric pocket of the active, closed state of the mutant IDH1 protein. Kinetic and/or structural studies have revealed that some mutant IDH1-targeted inhibitors may bind at the α-KG/isocitrate binding site (37, 48, 49), whereas others bind to the interface between the two protomers of the IDH1 dimer (50). The latter mechanism appears to involve a prevention of the catalysis by locking IDH enzymes in an open, pre-catalytic inactive conformation that is similar to that observed in the absence of α-KG or isocitrate and distinct from the closed conformation that can be observed when the α-KG/isocitrate site is occupied (33, 51). Although these two possibilities cannot be readily distinguished here regarding the actual mechanism of action of DOA, our computational approach favored the prediction that DOA might bind remotely and

thus allosterically alters the α-KG-binding catalytic pocket in the mutant IDH1 enzyme. For the allosteric cavity, most of the interactions performed between DOA and mutant IDH1 structures were found as key interacting residues; conversely, a majority of the interactions observed in the WT IDH1 crystallographic structure cannot be considered key residues, thus favoring the occurrence of a DOA binding mode preferentially for mutant IDH1 over WT IDH1. Indeed, because allosteric inhibitors of mutant IDH1 appear to operate by binding at the dimer interface, resulting in an open conformation and preventing the NADPH cofactor and substrate α-KG from coming close to the catalytic (Mg^{2+}) binding site, the fact that most of the best DOA binding energies were predicted to occur in closed conformations favors the notion that the inhibitory activity and selectivity of DOA might occur *via* allosteric targeting of the closed, active conformations of mutant IDH1. However, we cannot exclude the possibility that the DOA binding site at the orthosteric/catalytic cavity could overlap with that of α-KG to elicit a direct competition for the same binding site. The R132H 395G > A oncogenic IDH1 substitution is known to disrupt the substrate ability to reorganize the active site into the closed conformation, thereby leading to a gained affinity for the cofactor. In this regard, our computational studies predicted that DOA could directly interact with key residues at the disorganized active site induced by the R132H substitution, thus apparently targeting a key neomorphic vulnerability of mutant IDH1 enzymes similarly to BAY 1436032 (29). Moreover, in the conformation adopted by the 4KZ0 structure, DOA was predicted to likewise establish good binding energies with both the allosteric and the catalytic cavities of the mutant IDH1 enzymes, thus suggesting that DOA, which did not appear to exhibit structural similarities to any of the IDH inhibitors reported previously, could operate as a dual allosteric/orthosteric inhibitor of mutant IDH1.

As expected for a mutant IDH1-targeted drug, our biochemical studies revealed a good selectivity index of the inhibitory activity of DOA *in vitro*, which was >10-fold more active for the R132H IDH1 mutant than the WT IDH1 enzyme. Cell-based experiments confirmed that DOA's cellular activity was on par with the its observed activity against the purified form of the recombinant R132H IDH1 enzyme; DOA mimicked the highly potent and selective inhibitor of mutant IDH1 R132H/R132C AGI-5198 to strongly suppress the overproduction of 2HG in cells carrying a heterozygous knock-in R132H mutation. While this decrease in 2HG supported that DOA is cell membrane-permeable and *on target* (i.e., the mutant heterodimer IDH1 WT-R132H) in cells, another hallmark of IDH1-mutated cells is histone methylation, especially the 2HG-driven accumulation of trimethylation. Members of the jumonji lysine demethylase family, such as KDM4A–D, require α-KG as a co-substrate to catalyze the removal of methyl moieties on lysine and accumulated 2HG effectively inhibits this family of enzymes (44, 52). KDM4A–C each catalyzes demethylation of di- and tri-methylated H3K9

and H3K36, whereas KDM4D is specific for H3K9(me2/3). Previous studies have provided conflicting results regarding the effects of mutant IDH1-targeted inhibitors on methylation of histones, ranging from no changes to strong changes depending on the experimental model (15, 53). In our hands, however, under conditions of near-complete 2HG inhibition by DOA, we observed a drastic demethylation of H3K9me3. By reducing the intracellular concentration of 2HG, DOA can maintain the functions of histone demethylases and reverse the histone hypermethylation phenotype in MCF10A cells with an IDH1 R132H mutation. Indeed, the ability of DOA to target the neomorphic activity of mutant IDH1 apparently suffices to broadly correct the aberrant rewiring of multiple epigenetic layers in IDH1-mutated cells including not only histone modifications but also DNA methylation.

The so-called C5 or immunologically "quiet" subtype of cancer-associated immune landscapes, which is characterized by the lowest lymphocyte and highest macrophage responses, is enriched in IDH1 mutations, thus suggesting an association with 2HG overproduction, fewer tumor-associated immune cells and better outcome (54-56). Here, we hypothesized that if 2HG promotes DNA hypermethylation of *PD-L1* (23, 55), then reducing 2HG levels would enhance *PD-L1* expression *via* DNA demethylation. Accordingly, DOA's ability to impede mutant IDH1-driven overproduction of 2HG impacted the DNA methylation status responsible for the expression of *PD-L1*, a key regulator of the immune landscape of human tumors. When IDH1-mutant cells were treated with 5-aza to promote global demethylation, we observed an up-regulation of *PD-L1* expression that was exquisitely mimicked by DOA treatment. Moreover, the finding that DOA and AGI-5198 similarly increased the number of PD-L1-positive MCF10A$^{R132H/WT}$ cells, whereas DOA treatment was additionally capable of increasing PD-L1 protein content at the cell surface of MCF10A$^{R132H/WT}$ cells, suggests that the ultimate mechanism of action of DOA on PD-L1 expression could involve not only 2HG-related changes in active demethylation by TET enzymes, but also alteration of *de novo* methylation *via* direct blockade of DNMT enzymes (24). Nevertheless, our findings confirm that 2HG provides a direct conduit between IDH1 mutations and the epigenetic regulation of *PD-L1* expression in tumor cells (57-59), thereby supporting the notion that pharmacological correction of the supraphysiological levels of 2HG might play a key role in achieving IDH1-mutated tumor destruction through immunotherapy.

Considering the potential of DOA as a cancer therapeutic, we finally addressed the selective anti-tumor activity of DOA against mutant IDH1 tumor cells. Although we failed to observe short-term inhibition of cell viability or apparent early induction of cell death by DOA treatment, a slight but significant reduction in the long-term tumorigenic activity of IDH1-mutant cells became evident based on the noteworthy impact of DOA on colony formation potential. We should acknowledge that the ability of a heterogeneous cell population to

generate clones could be interpreted as a trait of aggressive tumor cell phenotypes, the so-called cancer stem cells (CSCs), which harbor tumor-initiating capabilities. Since CSCs are long-lived cells with the potential for strong survival and proliferation, determination of clonogenic growth can be used to evaluate the stemness of particular cell populations. In this regard, our findings suggest that DOA targets a 2HG-driven function that is relevant for maintenance of the CSC state within cell populations bearing an IDH1 mutation while largely sparing WT IDH1 isogenic counterparts. DOA-induced wide-scale reversion of aberrant epigenetic changes might unlock the 2HG-addicted undifferentiated state of CSCs to promote their differentiation into non-CSCs. Given that DOA treatment also reduced the expansion of colonies formed by a single, seeded CSC-like cell that harbored the ability for clonal growth, it appears that DOA could diminish the reproductive viability, that is, the capacity of 2HG-overproducing IDH1-mutant cells to produce progeny. Nevertheless, these *in vitro* studies should be revisited *in vivo* to validate date obtained from cell culture experiments. Previous experiments in our laboratory highlighted the ability of DOA to reduce the *in vivo* tumorigenicity of highly undifferentiated, CSC-like breast cancer cell populations (24). Because such approaches involved a pre-incubation of tumor cells with DOA before their injection in mice, more detailed preclinical and clinical studies on the expected low stability/bioavailability of EVOO oleosides (60,61) are urgently needed to understand their therapeutic limitations as well as to find the most appropriate delivery system to achieve the best efficiency level of DOA at the target tumor.

Several pharmacological inhibitors of the mutant form of IDH1 (e.g., AG-120, AG-221, AG-881, BAY1436032, IDG305) are progressing through phase I/II clinical trials in patients with AML or solid tumors, which highlights the fast progression from the first report of the IDH1 mutation less than 10 years ago to late phase clinical trials. However, as clinical studies continue, it is becoming increasingly evident that the successful eradication of IDH1-mutated tumors might require the blockade of additional molecules involved in 2HG-driven epigenetic and metabolic rewiring (*e.g.*, DNMTs and mTOR). Moreover, whereas fewer than ten chemotypes of mutant IDH-targeted inhibitors have been reported to date (47), we are already beginning to recognize mechanisms of acquired clinical resistance involving second-site *trans* and *cis* mutations that affect the interface of IDH dimers targeted by most of the available allosteric inhibitors (16). Here, we present evidence to suggest that a naturally occurring EVOO-derived polyphenol recently reported to targeted undifferentiated cell phenotypes with tumor-initiating capability by simultaneously inhibiting DNMT and mTOR activities (24), molecularly behaves as a new chemotype of mutant IDH1 inhibitors. Indeed, the Tanimoto and Dice indexes, two of the best methods to quantify the 2D/3D similarity of molecular representations (46) concluded that DOA structurally and physicochemically

behaved as a distant molecule compared with the existing mutant IDH1-specific inhibitors in the molecular space.

To the best of our knowledge, the phenol-conjugated oleoside DOA is the first natural compound reported to inhibit the neomorphic activity of mutant IDH1 enzyme, reduce 2HG oncometabolite production, reverse 2HG-driven epigenetic reprogramming such as histone/DNA hypermethylation, and decrease tumor-initiating capacity of mutant IDH1 cells. Although more detailed studies aimed at elucidating the precise mechanism of action of DOA are necessary before starting structure-guided lead optimization processes, IDH1-focused discovery campaigns should consider not only the investigation of mono-targeting mutant IDH1 pharmaceuticals, but also the multifaceted pharmacology that might arise from plant-derived phenolics such as DOA. The pharmacophoric structure of DOA might lead a multitarget-directed ligand strategy to develop single chemical entities that might be able to simultaneously modulate not only the neomorphic activity of mutant IDH1 enzymes, but also that of other enzymes (e.g., the mTOR/DNMT; **Fig. 6**) closely associated with the metabolo-epigenetic rewiring promoted by high cellular concentrations of 2HG, the hallmark of IDH1-mutant cancers.

Funding. This work was supported by grants from the Ministerio de Ciencia e Innovación (Grant SAF2016-80639-P to J. A. Menendez), Plan Nacional de I+D+I, Spain, and the Agència de Gestió d'Ajuts Universitaris i de Recerca (AGAUR) (Grant 2014 SGR229 to J. A. Menendez). This study was supported also by unrestricted research grants from Roche Pharma (Spain) and Astellas Pharma (Spain) to the Program Against Cancer Therapeutic Resistance (ProCURE, Catalan Institute of Oncology). Joaquim Bosch-Barrera is supported by SEOM, Pfizer (Grant WI190764), Boehringer Ingelheim, Meda Pharma, and Pla strategic de recerca i innovació en salut 2016–2020 de la Generalitat de Catalunya (SLT006/17/114). Elisabet Cuyàs is supported by the Sara Borrell post-doctoral contract (CD15/00033) from the Ministerio de Sanidad y Consumo, Fondo de Investigación Sanitaria, Spain.

Acknowledgments. The authors would like to thank Dr. Kenneth McCreath for editorial support.

Conflicts of interest. Authors have no competing interests to declare.

REFERENCES

1. Yang, H. et al. (2012) IDH1 and IDH2 mutations in tumorigenesis: mechanistic insights and clinical perspectives. Clin. Cancer Res., 18, 5562-5571.

2. Krell, D. et al. (2013) IDH mutations in tumorigenesis and their potential role as novel therapeutic targets. Future Oncol., 9, 1923-1935.

3. Cancer Genome Atlas Research Network (2015) The Molecular Taxonomy of Primary Prostate Cancer. Cell, 163, 1011-1025.

4. Clark, O. et al. (2016) Molecular Pathways: Isocitrate Dehydrogenase Mutations in Cancer. Clin. Cancer Res., 22, 1837-1842.

5. Dang, L. et al. (2016) IDH mutations in cancer and progress toward development of targeted therapeutics. Ann. Oncol., 27, 599-608.

6. Ye, D. et al. (2018) Metabolism, Activity, and Targeting of D- and L-2-Hydroxyglutarates. Trends Cancer, 4, 151-165.

7. Dang, L. et al. (2017) Isocitrate Dehydrogenase Mutation and (R)-2-Hydroxyglutarate: From Basic Discovery to Therapeutics Development. Annu. Rev. Biochem., 86, 305-331.

8. M Gagné, L. et al. (2017) Oncogenic Activities of IDH1/2 Mutations: From Epigenetics to Cellular Signaling. Trends Cell Biol., 27, 738-752.

9. Nowicki, S. et al. (2015) Oncometabolites: tailoring our genes. FEBS J., 282, 2796-2805.

10. Shim, E. H. et al. (2014). L-2-Hydroxyglutarate: an epigenetic modifier and putative oncometabolite in renal cancer. Cancer Discov., 4, 1290-1298.

11. Cairns, R. A. et al. (2013) Oncogenic isocitrate dehydrogenase mutations: mechanisms, models, and clinical opportunities. Cancer Discov., 3, 730-741.

12. Yang, M. et al. (2013) Oncometabolites: linking altered metabolism with cancer. J. Clin. Invest., 123, 3652-3658.

13. Menendez, J. A. et al. (2014) Gerometabolites: the pseudohypoxic aging side of cancer oncometabolites. Cell Cycle, 13, 699-709.

14. Waitkus, M. S. et al. (2018) Biological Role and Therapeutic Potential of IDH Mutations in Cancer. Cancer Cell, 2018 May 14. pii: S1535-6108(18)30182-X. doi: 10.1016/j.ccell.2018.04.011. [Epub ahead of print]

15. Tateishi, K. et al. (2015) Extreme Vulnerability of IDH1 Mutant Cancers to NAD+ Depletion. Cancer Cell, 28, 773-784.

16. Intlekofer, A. M. et al. (2018) Acquired resistance to IDH inhibition through trans or cis dimer-interface mutations. Nature, 2018 Jun 27. doi: 10.1038/s41586-018-0251-7. [Epub ahead of print]

17. Turcan, S. et al. (2013) Efficient induction of differentiation and growth inhibition in IDH1 mutant glioma cells by the DNMT Inhibitor Decitabine. Oncotarget, 4, 1729-1736.

18. Yang, Z. et al. (2017) 2-HG Inhibits Necroptosis by Stimulating DNMT1-Dependent Hypermethylation of the RIP3 Promoter. Cell Rep., 19, 1846-1857.

19. Carbonneau, M. et al. (2016) The oncometabolite 2-hydroxyglutarate activates the mTOR signalling pathway. Nat. Commun., 7, 12700.

20. Brat, D. J. et al. Comprehensive, Integrative Genomic Analysis of Diffuse Lower-Grade Gliomas. N. Engl. J. Med., 372, 2481-2498.

21. Bai, H. et al. (2016) Integrated genomic characterization of IDH1-mutant glioma malignant progression. Nat. Genet., 48, 59-66.

22. Wakimoto, H. et al. (2014) Targetable signaling pathway mutations are associated with malignant phenotype in IDH-mutant gliomas. Clin. Cancer Res., 20, 2898-2909.

23. Mu, L. et al. (2018) The IDH1 Mutation-Induced Oncometabolite, 2-Hydroxyglutarate, May Affect DNA Methylation and Expression of PD-L1 in Gliomas. Front. Mol. Neurosci., 11, 82.

24. Corominas-Faja, B. et al. (2018) Extra-virgin olive oil contains a metabolo-epigenetic inhibitor of cancer stem cells. Carcinogenesis, 39, 601-613.

25. Xu, X. et al. (2004) Structures of human cytosolic NADP-dependent isocitrate dehydrogenase reveal a novel self-regulatory mechanism of activity. J. Biol. Chem., 279, 33946-33957.

26. Deng, G. et al. (2015) Selective inhibition of mutant isocitrate dehydrogenase 1 (IDH1) via disruption of a metal binding network by an allosteric small molecule. J. Biol. Chem., 290, 762-774.

27. Pusch, S. et al. (2017) Pan-mutant IDH1 inhibitor BAY 1436032 for effective treatment of IDH1 mutant astrocytoma in vivo. Acta Neuropathol., 133, 629-644.

28. Dang, L. et al. (2009) Cancer-associated IDH1 mutations produce 2-hydroxyglutarate. Nature, 462, 739-744.

29. Cho, Y. S. et al. (2017) Discovery and Evaluation of Clinical Candidate IDH305, a Brain Penetrant Mutant IDH1 Inhibitor. ACS Med. Chem. Lett., 8, 1116-1121.

30. Levell, J. R. et al. (2016) Optimization of 3-Pyrimidin-4-yl-oxazolidin-2-ones as Allosteric and Mutant Specific Inhibitors of IDH1. ACS Med. Chem. Lett., 8,151-156.

31. Xie, X. et al. (2017) Allosteric Mutant IDH1 Inhibitors Reveal Mechanisms for IDH1 Mutant and Isoform Selectivity. Structure, 25, 506-513.

32. Okoye-Okafor, U. C. et al. (2015) New IDH1 mutant inhibitors for treatment of acute myeloid leukemia. Nat. Chem. Biol., 11, 878-886.

33. Yang, B. et al. (2010) Molecular mechanisms of "off-on switch" of activities of human IDH1 by tumor-associated mutation R132H. Cell Res., 20**,** 1188-1200.

34. Wu, F. et al. (2015) Inhibition of Cancer-Associated Mutant Isocitrate Dehydrogenases by 2-Thiohydantoin Compounds. J. Med. Chem. 58, 6899-6908.

35. Zheng, B. et al. (2013) Crystallographic Investigation and Selective Inhibition of Mutant Isocitrate Dehydrogenase. ACS Med. Chem. Lett., 4, 542-546.

36. Rendina, A. R. et al. (2013) Mutant IDH1 enhances the production of 2-hydroxyglutarate due to its kinetic mechanism. Biochemistry, 52, 4563-4577.

37. Cuyàs, E., et al. (2018) Metformin directly targets the H3K27me3 demethylase KDM6A/UTX. Aging Cell, 17, e12772.

38. Cuyàs, E. et al. (2015) Oncometabolic mutation IDH1 R132H confers a metformin-hypersensitive phenotype. Oncotarget, 6, 12279-12296.

39. Riera-Borrull, M. et al. (2016) Exploring the Process of Energy Generation in Pathophysiology by Targeted Metabolomics: Performance of a Simple and Quantitative Method. J. Am. Soc. Mass Spectrom., 27, 168-177.

40. Genheden, S. et al. (2015) The MM/PBSA and MM/GBSA methods to estimate ligand-binding affinities. Expert Opin. Drug Discov., 10, 449-461.

41. Duncan, C. G. et al. (2012) A heterozygous IDH1R132H/WT mutation induces genome-wide alterations in DNA methylation. Genome Res., 22, 2339-2355.

42. Lu, C. et al. (2012) IDH mutation impairs histone demethylation and results in a block to cell differentiation. Nature, 483, 474-478.

43. Richarson, A. D. et al. (2016) Registered report: IDH mutation impairs histone demethylation and results in a block to cell differentiation. Elife, 5, e10860.

44. Chowdhury, R. et al. (2011) The oncometabolite 2-hydroxyglutarate inhibits histone lysine demethylases. EMBO Rep., 12, 463-469.

45. Nigsch, F. et al. (2008) How to winnow actives from inactives: introducing molecular ortogonal sparse bigrams (MOSBs) and multiclass Winnow. J. Chem. Inf. Model, 48, 306-318.

46. Bajusz, D. et al. (2015) Why is Tanimoto index an appropriate choice for fingerprint-based similarity calculations? J. Cheminform., 7, 20.

47. Madala, H. R. et al. (2018) Beyond Brooding on Oncometabolite Havoc in IDH-Mutant Gliomas and AML: Current and Future Therapeutic Strategies. Cancers (Basel), 10(2), pii: E49.

48. Popovici-Muller, J. et al. (2012). Discovery of the First Potent Inhibitors of Mutant IDH1 That Lower Tumor 2-HG in Vivo. ACS Med. Chem. Lett., 3, 850-855.

49. Davis, M. I. et al. (2014) Biochemical, cellular, and biophysical characterization of a potent inhibitor of mutant isocitrate dehydrogenase IDH1. J. Biol. Chem., 289, 13717-13725.

50. Wang, F. et al. (2013) Targeted inhibition of mutant IDH2 in leukemia cells induces cellular differentiation. Science, 340, 622-626.

51. Zhao, S. et al. (2010) IDH1 mutant structures reveal a mechanism of dominant inhibition. Cell Res., 20, 1279-1281.

52. Xu, W. et al. (2011) Oncometabolite 2-hydroxyglutarate is a competitive inhibitor of α-ketoglutarate-dependent dioxygenases. Cancer Cell, 19, 17-30.

53. Rohle, D. et al. (2013) An inhibitor of mutant IDH1 delays growth and promotes differentiation of glioma cells. Science, 340, 626-30.

54. Amankulor, N. M. et al. (2017) Mutant IDH1 regulates the tumor-associated immune system in gliomas. Genes Dev., 31, 774-786.

55. Venteicher AS et al. (2017) Decoupling genetics, lineages, and microenvironment in IDH-mutant gliomas by single-cell RNA-seq. Science, 355(6332).

56. Thorsson, V. et al. (2018) The Immune Landscape of Cancer. Immunity, 48, 812-830.e14.

57. Berghoff, A. S. et al. (2017) Correlation of immune phenotype with IDH mutation in diffuse glioma. Neuro Oncol., 19, 1460-1468.

58. Lucca, L. E. et al. (2017) Resisting fatal attraction: a glioma oncometabolite prevents CD8+ T cell recruitment. J. Clin. Invest., 127, 1218-1220.

59. Kohanbash, G. et al. (2017) Isocitrate dehydrogenase mutations suppress STAT1 and CD8+ T cell accumulation in gliomas. J. Clin. Invest., 127, 1425-1437.

60. Vazquez-Martin, A. et al. (2012) Phenolic secoiridoids in extra virgin olive oil impede fibrogenic and oncogenic epithelial-to-mesenchymal transition: extra virgin olive oil as a source of novel antiaging phytochemicals. Rejuvenation Res.,15, 3-21.

61. García-Villalba, R. et al. (2012) Uptake and metabolism of olive oil polyphenols in human breast cancer cells using nano-liquid chromatography coupled to electrospray ionization-time of flight-mass spectrometry. J. Chromatogr. B Analyt. Technol. Biomed. Life Sci., 898, 69-77.

FIGURE LEGENDS

Figure 1. Binding mode of DOA to mutant and wild-type IDH1. A. *Top left*. Global view of a mutant IDH1 homodimer structure showing the location of the allosteric domain and the α-KG and NADPH pockets at the orthosteric/catalytic domain. *Top right.* Figure shows in sticks all the pharmacophoric interaction residues involved in the predicted *in silico* binding of DOA to the orthosteric and allosteric domains of wild-type (WT) and mutant IDH1 proteins, using PLIP. Orange dashed lines represent hydrogen bond interactions; gray dashed lines represent hydrophobic interactions. The main residues involved in DOA interaction with the protein backbone are shown in black; the residue numbers shown correspond to the original PDB file numbering. Panels correspond to self-docking posses under molecular dynamics (MD) simulations modeling the backbone and ligand (DOA) flexibility. *Bottom.* Global view of IDH1 structures showing a detailed location of the DOA binding sites at the orthosteric and allosteric cavities. **B.** Steered MD force profiles to show the different peaks formed when DOA was pulled out from the orthosteric (*top*), allosteric (*middle*), and orthosteric/allosteric (*bottom*) cavities of either WT-IDH1 (1T0L) or mutant IDH1 (3MAP, 4L04) proteins.

Figure 2. DOA selectively inhibits mutant IDH1 activity *in vitro*. A. *Upper-left.* Schematic of wild-type (WT)-IDH1 and mutant IDH1 enzymatic reactions. *Bottom-left.* Dose-response analyses show the inhibitory effects of DOA on the activity of purified WT-IDH1 and R132H IDH1 enzymes. *Columns* and *error bars* represent mean values and S.D., respectively. Comparisons of means were performed by ANOVA *P* values < 0.05 and <0.005 were considered to be statistically significant (denoted as * and **, respectively). *Right.* Inhibition percentage of WT-IDH1 and mutant IDH1 enzymatic activity in the presence of graded concentrations of DOA. IC_{50} values were calculated from concentration-effect curves by interpolation. **B.** *Left.* Quantification of 2HG levels (expressed as normalized OD_{450} values) in whole cell lysates obtained from $MCF10A^{WT/WT}$ and $MCF10A^{R132H/WT}$ cells treated with DOA or AGI-5198 during 2 days with daily refeed. *Columns* and *error bars* represent mean values and S.D., respectively. Comparisons of means were performed by ANOVA. *P* values < 0.005 were considered to be statistically significant (denoted as *). *Right.* A combined mass spectrum of the region where 2HG was eluted (m/z 349.1317) in base-peak chromatograms of extracts from $MCF10A^{WT/WT}$ and $MCF10A^{R132H/WT}$ cells treated with DOA during 2 days with daily refeed is shown (four technical replicates per n; n=3 biological replicates). *Columns* and *error bars* represent mean values of 2HG levels (μmol/L mg^{-1}) and S.D., respectively. Comparisons of means were performed by ANOVA. *P* values < 0.05 were considered to be statistically significant (denoted as *).

Figure 3. DOA reverses 2HG-driven epigenetic rewiring in mutant IDH1 cells. A. *Left.* Representative immunoblots for H3K9me3 histone modification in whole cell lysates obtained from MCF10A$^{WT/WT}$ and MCF10A$^{R132H/WT}$ cells treated with 50 μmol/L DOA during 2 days with daily refeed. Also shown are β-actin loading controls. *Right.* Immunofluorescence images show portions of MCF10A$^{WT/WT}$ and MCF10A$^{R132H/WT}$ cell cultures after exposure to graded concentrations of DOA for 48 h and captured in different channels for H3K9me3 (green) and Hoechst 33258 (blue) with a ×20 objective. Figure shows representative immunofluorescence microphotographs of at least 3 independent experiments performed in triplicate. **B.** *Upper-left.* Total RNA from MCF10A$^{WT/WT}$ and MCF10A$^{R132H/WT}$ cells cultured in the absence or presence of 5-azacytidine or DOA was characterized in technical replicates for the relative abundance of *PD-L1* mRNA. The transcript abundance was calculated using the delta Ct method and presented as fold-change *versus* basal expression in MCF10A$^{WT/WT}$ parental cells. *Bottom-left.* Representative flow cytometry histograms showing the mean fluorescence intensity (MFI) of cell surface-associated PD-L1 in MCF10A$^{WT/WT}$ and MCF10A$^{R132H/WT}$ cells under standard culture conditions. *Right.* Representative flow cytometry dot plot graphs obtained from three independent experiments showing the percentage of PD-L1-positive cells in MCF10A$^{WT/WT}$ and MCF10A$^{R132H/WT}$ cell populations following exposure to AGI-5198 or DOA for 2 d with daily refeed.

Figure 4. DOA selectively targets mutant IDH1-driven tumorigenicity. Representative photographs from 6-well plates of colonies of MCF10A$^{WT/WT}$ and MCF10A$^{R132H/WT}$ cells treated with DOA and AGI-5198. ImageJ (NIH) was used to quantify the number (*top panels*) and size (*bottom panels*, central lines indicate mean values ± SD) of 7 day-old colonies stained with crystal violet. *Columns* and *error bars* represent mean values and S.D., respectively. Comparisons of means were performed by ANOVA. *P* values < 0.05 were considered to be statistically significant (denoted as *).

Figure 5. DOA is a new chemotype of mutant IDH1-targeted inhibitors. *Left.* Chemical structures of IDH1 substrates (isocitrate [ICT], citrate anion [FLC], α-ketoglutarate [AKG]), IDH1 cofactors (NADPH [NDP], NADP+ [NAP]), and a broad representation of currently existing mutant IDH1-targeted inhibitors. *Right.* Figure shows 2D (*top*) and 3D (*bottom*) molecular similarity matrices for pairwise comparison between DOA and IDH1/2-targeted molecules. Dice and Tanimoto similarity coefficients were calculated as the weighted average of the outcomes of the Atom pair, topological torsion, and Morgan/circular molecular fingerprints employed to computational encode the structure and properties in a given compound. Also, 3D similarity coefficients were calculated based on a combination of molecular shape complementarity and pharmacophoric features in the 3D space.

Figure 6. DOA: A novel inhibitor of cancer-associated mutant IDH1. *Upper-left.* Schematic of the DOA-driven suppression of 2HG-enhanced trimethylation of

H3K9me3 in mutant IDH1 cells. *Upper-right.* Working model schematic of the DOA-driven suppression of 2HG-enhanced hypermethylation of the *PD-L1* gene promoter in mutant IDH1 cells. *Bottom.* Wild-type IDH1 catalyzes the conversion of isocitrate to α-KG using the cofactor $NADP^+$ (*top-left* panel). Heterozygous mutations of IDH1 reduce normal enzymatic activity, but confer also a neomorphic (gain-of-function) activity that promotes conversion of α-KG to D-hydroxyglutarate (2HG) in a NADPH-dependent manner (*top-right* panel). α-KG and 2HG share high structural similarity, allowing 2HG to bind and inhibit α-KG-dependent enzyme activity including that of the jumonji lysine demethylase (KDM) family and the Ten-eleven translocation (TET) family of 5-methylcytosine hydroxylases (*bottom-left* panel). Consequently, inhibition of α-KG-dependent KDMs and TETs by 2HG causes profound epigenetic changes in the so-called hypermethylation phenotype, which promotes a stem-like cell differentiation block that contributes to malignant transformation (*bottom-right* panel). Although multiple inhibitors of mutant IDH1 (mIDH1i) have been developed and are in clinical testing, we are beginning to appreciate that pharmacological depletion of 2HG might not be sufficient to inhibit the growth of several IDH1-mutated solid cancer types. These findings suggest that additional metabolic and/or epigenetic factors may modulate the therapeutic effect of direct mIDH1 inhibition. On the one hand, IDH1 mutations, which occur at the earliest stages of tumorigenesis, alter canonical metabolic pathways (e.g., glutamine catabolism, mitochondrial Krebs cycle, and mTOR) in a manner that facilitates the occurrence and later selection of additional driver mutations (PI3K/AKT, MET, KRAS, among others). On the other hand, only minimal alterations in global epigenetic changes and moderate inhibition of IDH1 mutant tumor growth have been reported despite near-complete abrogation of 2HG overproduction, thus suggesting that the maintenance of hypermethylated epi-phenotypes should involve additional chromatin-modifying enzymes (e.g. DNMTs). We now report that the oleoside decarboxymethyl oleuropein aglycone (DOA), a phenol-conjugated secoiridoid naturally present in the minority fraction of extra virgin olive oil, which has been shown to target the key phenotypic traits commonly observed in IDH1-mutant tumors such as stem-like undifferentiated cellular states and epigenetically suppressed differentiation programs (24), is a new chemotype of mutant IDH1-targeted inhibitors. The multitarget-directed ligand nature of DOA, which has been shown to target mTOR and DNMTs (24), might therefore provide a novel, multifaceted approach against IDH1-mutant cancers.

Figure 1

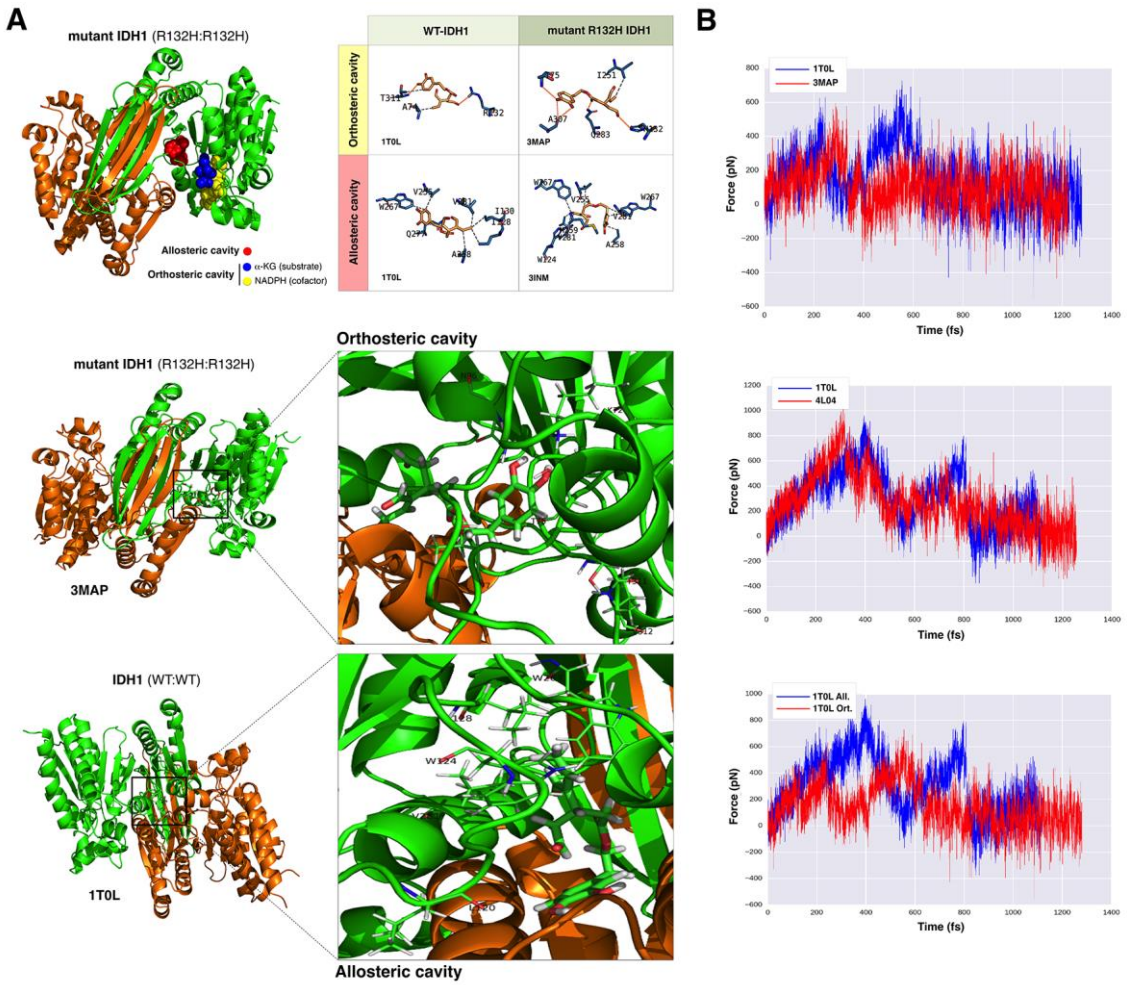

Figure 2

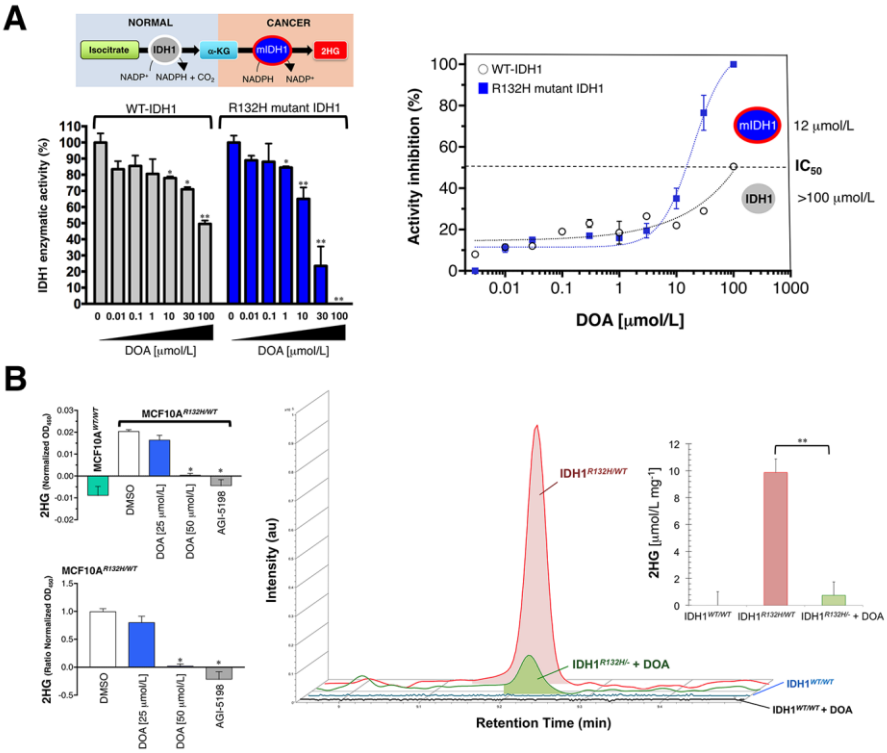

Figure 3

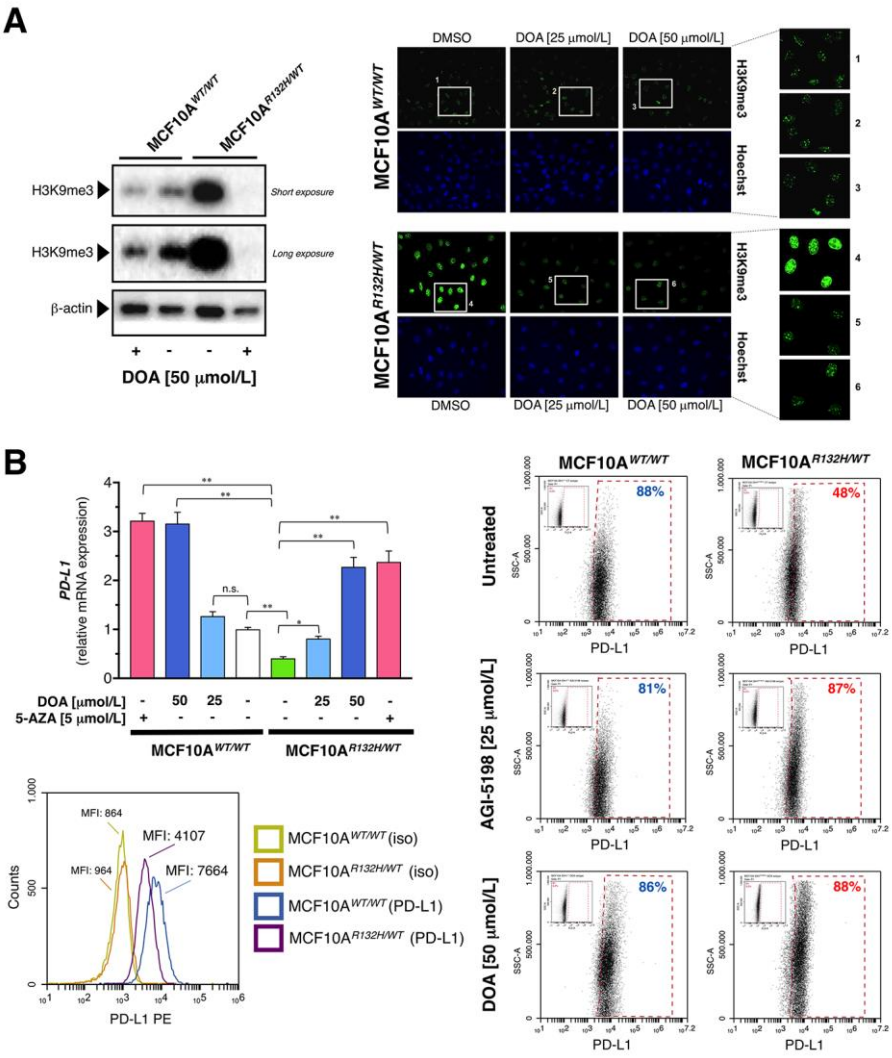

Figure 4

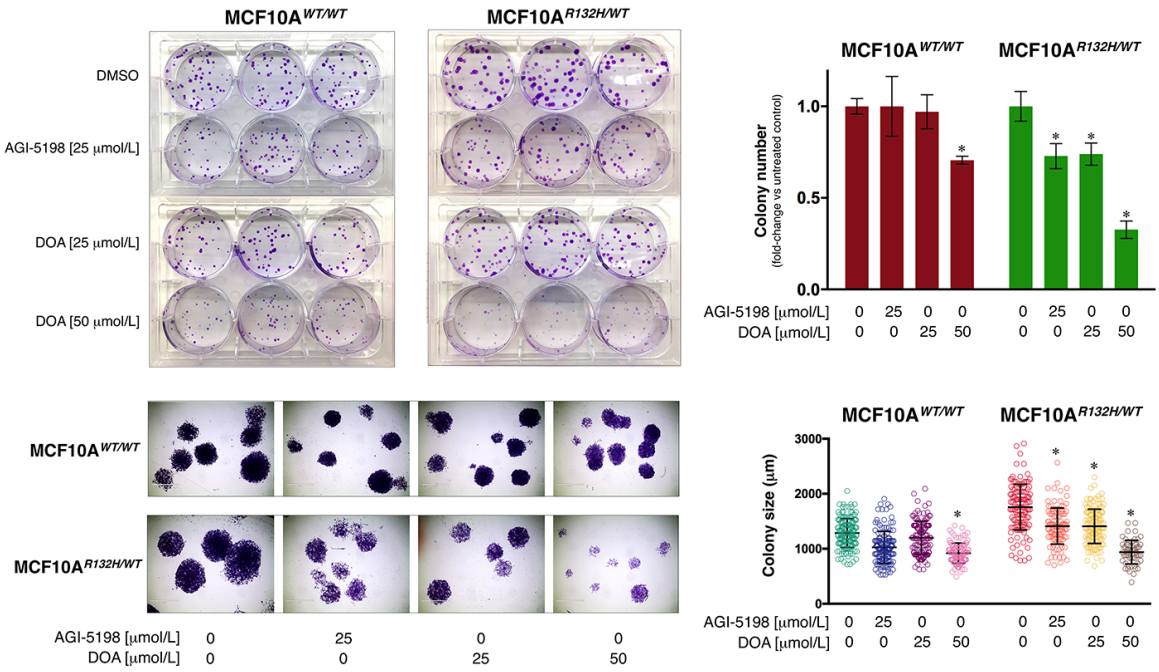

Figure 5

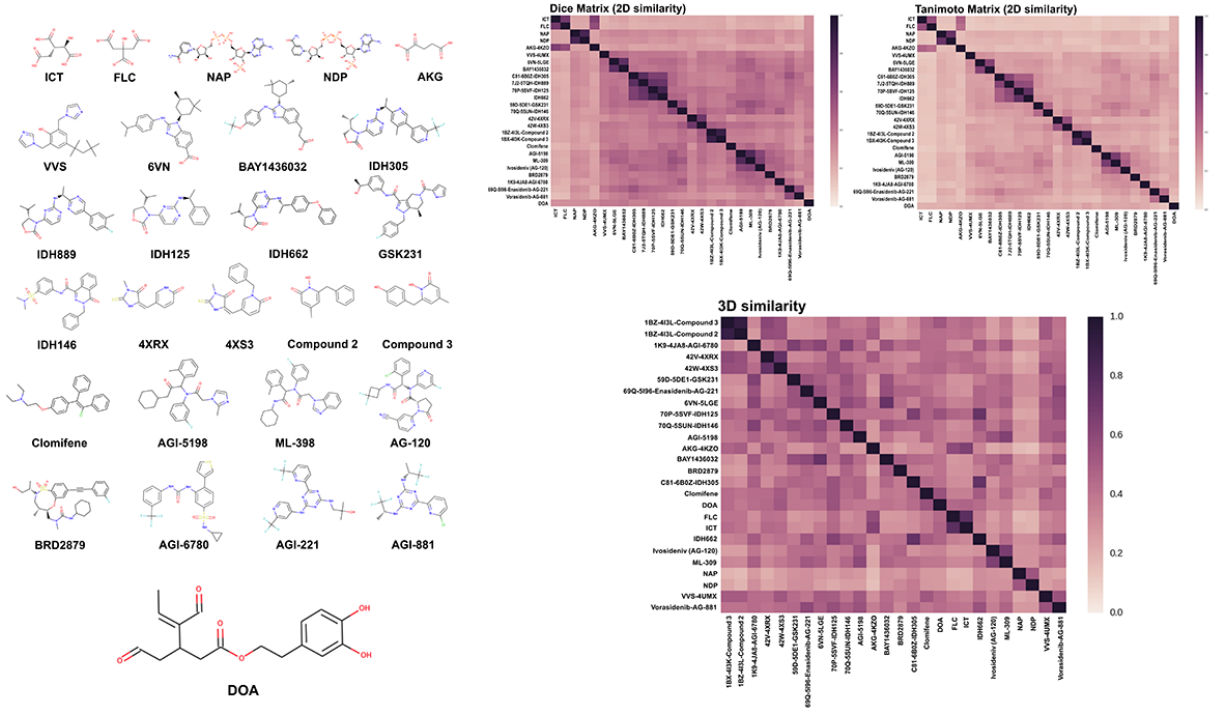

Figure 6